Manuscript to be submitted to International Journal of Aeroacoustics

Identification of Noise sources in a Rocket Engine Test Stand using Microphone Phased Array

Jayanta Panda
NASA Ames Research Center, Moffett Field, CA

Evan D. Crowe
Metis Technologies, Moffett Field, CA

Lester A. Langford
NASA John C. Stennis Space Center, MS

Earl T. Daley
NASA Ames Research Center, Moffett Field, CA

K. R. Hamm, Jr.
NASA Ames Research Center, Moffett Field, CA

Joel W. Sills Jr.
NASA Johnson Space Center, TX

Abstract

A new, phased array of microphones, suitable for the harsh environment of a rocket launch, was built and tested during a static firing of a RS-25 engine. It uses 70 piezo-resistive, dynamic pressure sensors, optimally distributed on a 10.5ft diameter open frame dome structure, and has a 200-ft long cable bundle to carry the signals to a weather-protected cabinet containing the data systems. The test stand was imaged using an infra-red camera and a visible wavelength camera, and the beamformed noise maps were superimposed on the photographs. The first-time data from a full-scale engine test stand showed that the plume deflector at the bottom of the engine to be the primary noise source. The openings of the test stand around the nozzle exit were also found to be noise sources particularly at higher frequencies. The final goal is to use the array during NASA's Artemis-II launch at Kennedy Space Center.

I. Nomenclature:

b: Beamformed output

w: Steering vector

p: pressure

c = speed of sound

k = wavenumber = $2\pi f / c$

N, N_s = No of grid points in the viewing region

u: Eigenvector

σ: Eigenvalues

Σ*:* Matrix of eigenvalues

φ: Phase

G: Cross-spectral matrix

Φ, θ : Angular separation from speaker sources.

M = Total no of microphones

St = Strouhal frequency

λ = Wavelength

d = Aperture of the array

f = Frequency

t: time

TH: Train Horn

SEM: Spectral Element Method

CB: conventional beamform

FB: functional beamform

LRAD: Long-Range Acoustic Device

Superscripts:

† = Complex-conjugate and transpose

* = Complex conjugate only

T = Transpose only

mod = model

v : Exponent of functional beamforming

Subscripts:

c = center of the array

j = index for interrogation grid

m = microphone index

R = Rayleigh resolution

t: total

s: desired sound source

b: background noise

e: electronic noise

sb: combination of desired and background noise

II. INTRODUCTION

Every part of a launch vehicle, launch pad, and ground operation equipment is subjected to the high acoustic load generated during lift-off [1]. The acoustic load is a major contributor to the vibro-acoustics environment to which every payload, vehicle structure, propellant storage and handling devices, and electronics and navigational component must be designed, tested and certified. Even a single decibel reduction of the acoustic levels translates into a sizable reduction of acoustic loadings, certification costs, operation costs and even vehicle weight. The same is true for every payload that the vehicle carries. Therefore, lowering of the acoustic level via various mitigation schemes is an important aspect of a launch pad design. The first step is the identification of the sources responsible for noise generation. Typically, single microphones are placed at different locations on a launch pad and on the vehicle to measure acoustic fluctuations. Such microphones, however, are unable to determine the noise sources. Single microphones provide a measure of the absolute level, leaving the cause of noise generation to speculation. In contrast, a phased array of microphones directly identifies the locations and relative strengths of the noise sources and is therefore capable of providing significant insights into

the underlying cause. Effectively a phased array acts as a “tuned ear,” or a “sound camera” capable of finding the highest sound generating regions.

Another advantage of a phased array is its ability to “see” through the smoke, water vapor and dust cloud generated during a rocket launch. While the view of the pad becomes obscured by this cloud the sound waves pass through. This allows for the identification of the noise sources at all phases of the launch from hold-down to elevation above the launch tower. A third advantage of a phased array is its ability to identify regions of the pad affected by the splashing of the rocket plumes as the vehicle ascends from the hold-down state. The zones affected by the plume impingement are typically locations of louder noise sources and are easily identifiable by a phased array [2, 3]. The plume impingement zones can create thermal damage to the launch platform. To mitigate such thermal damage and to reduce the acoustic environment many launch pads for heavy-lift rocket vehicles employ extensive water suppression systems. A knowledge of the distribution of the acoustic sources at every stage of the launch provides actionable information to optimize the water suppression system. An important goal of the present effort is to determine the plume splashing regions on the Launchpad via acoustic source identification.

The benefits of a phased array were demonstrated earlier in the static-burn tests [2], and in the static engine test and the first launch of the Northrop Grumman’s Antares vehicle [3]. In the recent past phased array proved to be a valuable tool to redesign the launch pads of Ariane [4] and Vega [5] vehicles.

The present array is a new design based on various lessons learnt from the past applications [2, 3]. Two important ones are the need for an open frame design to better sustain the wind and blast loads, and the use of piezo-resistive microphones that are better suited for the salty air of a typical launch site. The array was designed, fabricated, and tested (using speaker sources) at NASA Ames [1]. It was then transported to NASA Stennis Space Center to participate in the hot-firing test of an RS-25 engine. The goals were: (a) to determine the beamforming ability of the array in realistic environment; (b) determine tolerance to the weather elements, and (c) to gain experience with the logistics of operation, such as lifting and mounting, disassembly and reassembly of hardware, optimum procedure for data collection etc. The data provided insights into the noise sources around a full-scale engine test stand. The Stennis test is a part of a planned series of Validation and Verification (V&V) tests that makes the path towards the final deployment during Artemis-II launch.

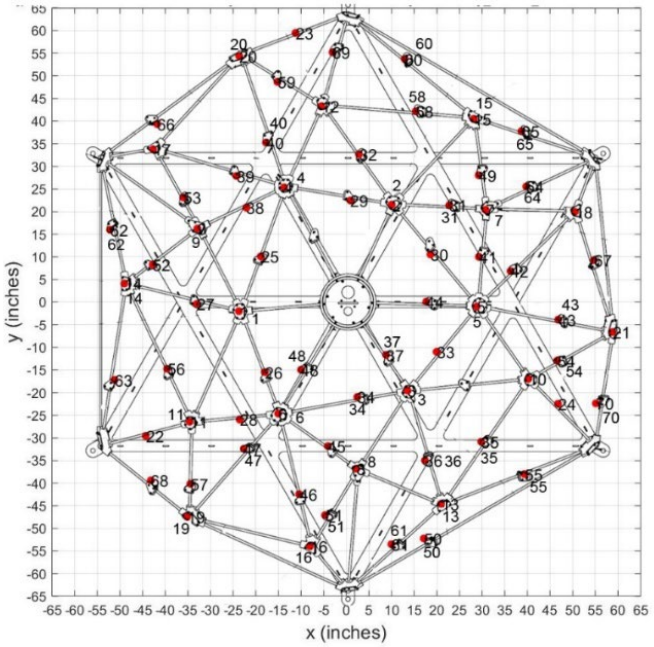

Fig 1. Location and numbering of Microphones.

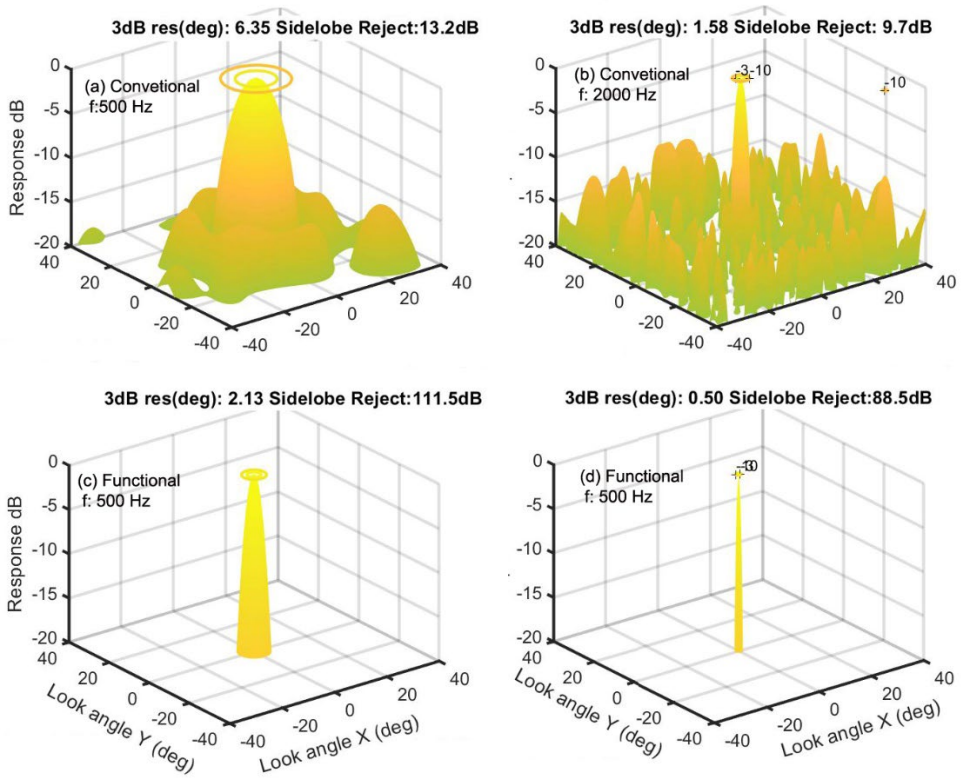

Fig 2. Ideal sound map (point spread function) created by the array at the indicated frequencies and using conventional and functional beamforming methods from a sound source located along the line of sight and 500-ft away from the array.

Fig 3. Overall view of the phased array, cable bundle, and data acquisition cabinet.

III. ARRAY HARDWARE

The custom-built, one-of-a-kind, phased array uses 70 dynamic pressure (Kullite) sensors laid out in a predetermined arrangement (fig 2). The goal of the layout is to maximize the array resolution at 500Hz ≤ f ≤ 2 kHz range, and to reduce the side lobes (fake noise sources) in the resulting sound maps. To design the layout the locations were first determined on a two-dimensional base circle of 62.7" radius; subsequently they were raised on a hemispherical surface with 88.67" radius. Inside the base circle 24 of the microphones were positioned on logarithmic spirals and the rest were randomly scattered. The resulting pattern produces a narrow point-spread function (psf), Fig 3 shows the ideal array response at two different frequencies using two different methods of analysis.

For conventional beamforming the minimum resolvable detail is due to the diffraction-limit of the array, i.e., when the first diffraction minimum of the image of one source point coincides with the maximum of another. For a circular aperture of diameter d, the Rayleigh resolution in radian θ_R is as following:

$$sin\theta_R = 1.22\ \frac{\lambda}{d} \quad \textbf{(1)}$$

The conventional beamform created large 3dB spot sizes of 6.38° and 1.58° at 500Hz and 2 kHz, respectively. The spot sizes are close to the predicted value from the Rayleigh criteria of eq. 1. The functional beamform processing created spot sizes smaller by a factor of ~3: 2.13° and 0.5° for the same two frequencies. The side-lobe rejection also improved significantly. These beamform models will

be described in the next section. A goal of the present work was to determine if such reductions were attainable in actual tests.

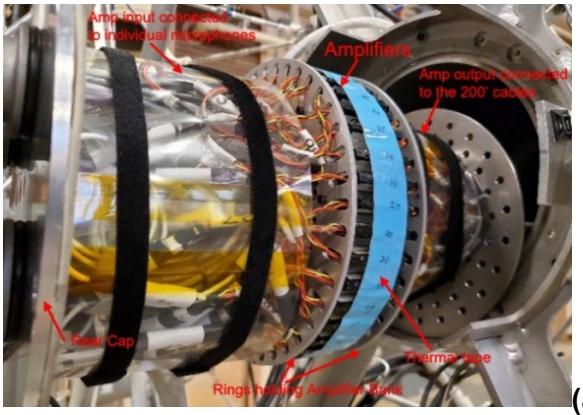

(a)

(b)

Fig 4. (a) Amplifier rack with amplifiers installed; (b) cameras mounted on the front cap.

Figure 4 shows a photograph of the newly built phased array with its three primary components: (a) the hemispherical dome shaped lattice structure that holds 70 dynamic pressure sensors, (b) a 200-ft long cable bundle, and (c) an air-conditioned cabinet to hold all electronic components and computers. The cylinder (also known as the canister) at the center of the dome structure holds one visible wavelength video camera, and a long infra-red wavelength (2micron- 10micron meter) video camera (fig 5b). A glass and a Germanium window, placed on the front cap, provide clear view of the launch pad and the vehicle in the visible and infra-red wavelengths, respectively. Additionally, amplifiers for all 70 microphones are also housed inside the canister (fig 5a). To monitor the temperature of the amplifier-rack a resistance temperature detector (RTD) is attached to the amplifier housing. Additionally, a three-axis accelerometer is placed on the mounting rod for the amplifier rack to monitor the vibration levels expected during the launch. Finally, a ½-inch diameter tube is placed close to the amplifier housing to bring in dry air to cool the amplifiers, and to maintain a low humidity environment at the interior of the canister. The array is expected to be mounted close to a launch pad weeks before the actual launch with little access. The cooling air will limit the temperature and humidity rise inside the canister.

A more detail description of the array hardware can be found in ref [6]. The cable bundle passes DC power and signals to and from the array dome to the data acquisition cabinet. The 200-ft long cable bundle is suitable for raising and mounting the array on nearby tall structures (such as lightening towers, water tanks or any other suitable structure) so that a clear view of the top surface of the launch platform becomes visible to the array cameras. The data acquisition cabinet holds a 24-bit primary and 16-bit backup data acquisition systems to digitize the microphone and the accelerometer signals. Data was collected at a rate of 20480 samples/s, and the IR camera images at 12.5frames/s. The cabinet is

made of steel for protection from the launch environment. It also has an air-conditioning unit to cool all electronics during the expected multiple weeks of continuous operation in the hot sun.

The hemispherical shape of the array dome and the triangular lattice frames are known to produce structural stiffness while minimizing the overall weight. The lattice structure was inspired by a similar dome shaped array built by Burnside and Horne [7] for use in a wind tunnel. Prior acoustic phased arrays [2, 3] used for the rocket launch studies had solid cross-section areas, which caused them to catch the overpressure and the acoustic waves from rocket launches creating large vibrational responses. The present design allows for the minimization of the wind and acoustic loadings and is expected to have much less vibration response. This was confirmed from multiple load analysis and calculations of the modal response of the frame.

The acoustic sensors on the phased array are piezo-resistive dynamic pressure sensors manufactured by Kulite Corporation. There are three different types of sensors on the phased array: larger 0.15” diameter XTEH-10L-190S-25A, and XTL-190-25A, and miniature 0.072” diameter XCL-072-25A. All are of absolute pressure gauges with 25psia range and produce full-scale output of 0-5V. The sensors were tested in a jet flow facility to ensure phase matching. The microphones were approximately mounted based on the designed location. The exact locations were established after the completion of the dome assembly and mounting. A photogrammetry-based technique using a V-STARS instrument (of Geodetic Systems) was used for this purpose. A single camera was used to take many photographs of the array, reference points, and guide poles and markers mounted on and around the array. Later on, a proprietary software was used to extract the microphone coordinates to an accuracy less than ±0.01”.

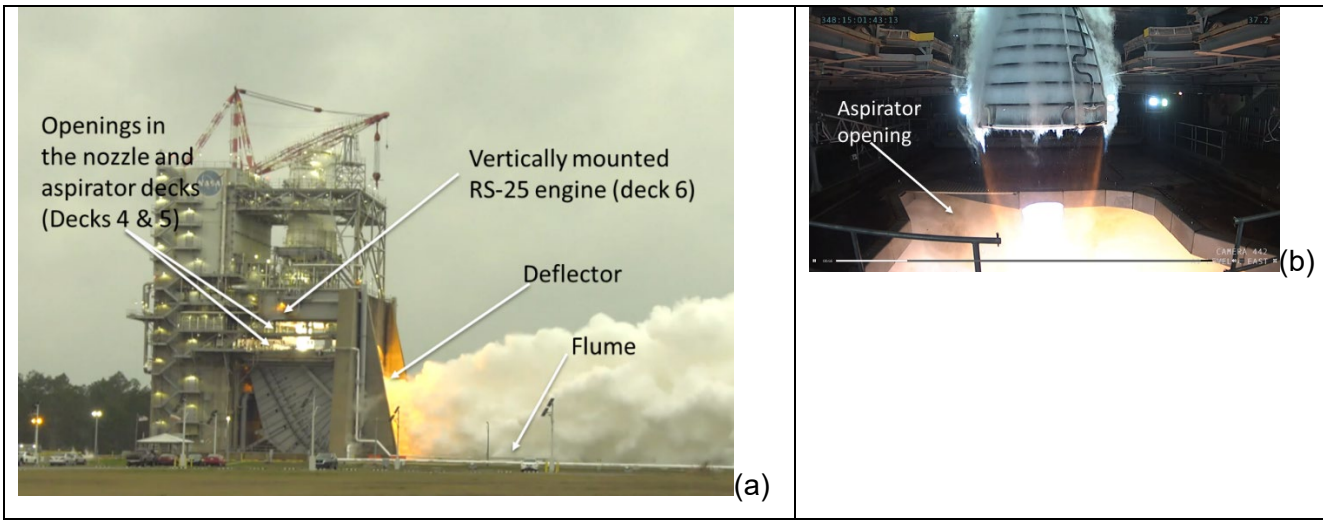

Fig 5. (a) photograph of the Fred Haise (A-1) engine test stand during RS-25 engine burn; (b) plume from the nozzle passing through the aspirator opening in deck 4.

(a)

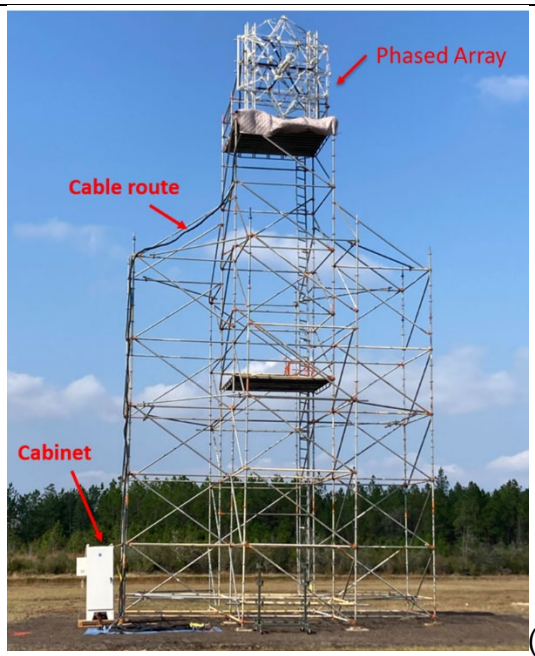

(b)

Fig 6. (a) Location of the array with respect to the test stand; (b) scaffold to hold the array hardware.

IV. TEST SETUP

The RS-25 engine static firing provided a good opportunity to test the array in a realistic environment. The engine was tested in the A-1 Test Stand of NASA Stennis Space Center. It is a single-position, vertical-firing facility where an engine is held above the 5th deck (fig 5a) and is supplied with liquefied Hydrogen and Oxygen. The plume out of the nozzle (fig 5b) passes through an “aspirator opening” on the 4th deck and impinges on a J-deflector. The flame deflector is made up of 21 stacked angular segments – or water boxes – each drilled with a pattern of holes to direct water as needed to cool the stand’s flame deflector. As much as 170,000 gallons of water per minute at 225 pounds per square inch pressure is supplied to the A-1 Test Stand during a test. The water is primarily used to cool the flame deflector and to keep it undamaged as it redirects engine exhaust [8]. The steam and the plume mixture flow out horizontally over an open channel flume.

The array was placed on the west side, and 460ft away from the test stand (fig 6a). The distance is comparable to the proposed separation in the Artemis application. A 50-ft tall scaffold structure was built, and the array dome was hoisted and mounted atop the scaffold. The dome was oriented to face the test stand. From the 50-ft height the cameras inside the array had unobstructed view of the entire test stand and a part of the flume. A part of the cable bundle was routed along the side of the scaffold and the data acquisition cabinet was placed at the base. The cabinet was supplied with electrical power, cooling air, and Ethernet connection for remote operation of the data acquisition computers. In addition, an engine start-stop signal was supplied for simultaneous recoding with the microphone data.

V. PHASED ARRAY DATA PROCESSING

Fundamentally a phased array detects the curvature of the acoustic waves to determine the angular location of the noise sources. The information is extracted via calculating cross-spectrum of pressure fluctuations between every possible pair of microphones on the array. In addition to the desired sound signals $p_{m,s}(t)$ the time-signal generated by the microphones $p_{m,t}(t)$ carries two different sources of noise. For the piezo-resistive sensors used in the present array the electronic noise is high. Even for the 24-bit data system the equivalent acoustic pressure $p_{m,e}(t)$ was around 105dB. Additionally, for launch acoustics application there are host of weaker spurious sources that create background fluctuations $p_{m,b}(t)$. For example, the pressure fluctuations from the strong wind blowing on the array can be 100dB or higher. There are weaker sound sources such as valve and gas flow generated noise, and reflections of various kinds that contaminate the measured pressure fluctuations $p_m(t)$. Let m = 1, 2, …M be indices for microphones, then the following holds for the total fluctuations measured by the m^{th} microphone:

$$p_{m,t}(t) = p_{m,s}(t) + p_{m,b}(t) + p_{m,e}(t) \quad \textbf{(2)}$$

Assuming that $\mathrm{p_{m,s}(t)}$, $\mathrm{p_{m,b}(t)}$, and $\mathrm{p_{m,e}(t)}$ are mutually uncorrelated and stationary, the following relationship holds for the cross spectrum between a microphone pair m and $m^{/}$ [9]:

$$G_{mm^{/},t} = \langle P_{m,t}{}^{*} P_{m^{/},t} \rangle = G_{mm^{/},s} + G_{mm^{/},b} + G_{mm^{/},e} \quad \textbf{(3)}$$

The contribution from the electronic noise can be subtracted by taking a set of data $p_{m,e}(t)$ at an indoor condition with the sound sources turned off, and then by calculating the noise-induced cross spectrum $G_{mm^{/},e}$ for every pair of microphones.

$$G_{mm^{/},e} = \langle P_{m,e}{}^{*} P_{m^{/},e} \rangle \quad \textbf{(4)}$$

Direct subtraction of the noise cross-spectra from the total measured was found to be problematic for the beamformed map since the phase spectrum became contaminated by the random noise of the former spectra. Therefore, only the magnitude of the noise-induced cross-spectrum was subtracted from that of the total measured, leaving the phase part intact:

$$G_{mm^{/},t}(f) = \left|G_{mm^{/},t}\right| e^{-i\,\mathrm{f}\,\Phi_{mm^{/}}}$$

$$G_{mm^{/},sb}(f) = \left(\left|G_{mm^{/},t}\right| - \left|G_{mm^{/},e}\right|\right) e^{-i\,\mathrm{f}\,\Phi_{mm^{/}}} \quad \textbf{(5)}$$

The resulting $G_{mm^{/},sb}(f)$ is the cross-spectrum from the combination of the desired sound sources and the background noise.

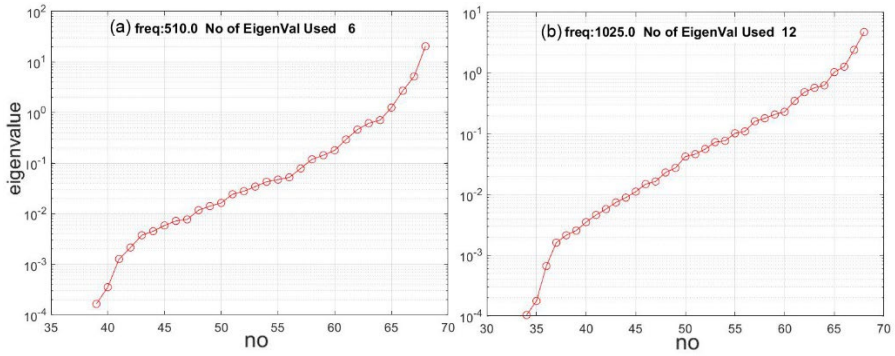

Fig 7. Eigenvalues of the cross-spectral matrix $G_{mm',sb}(f)$ at indicated two frequencies from the test data.

To further reduce the influence of the background noise for the Functional beamform scheme, the eigenvalues of the $\boldsymbol{G_{mm',sb}}$ matrix was inspected via an eigenvalue decomposition:

$$\boldsymbol{G_{sb}} = \boldsymbol{U\Sigma U}^* = \sum_{m=1}^{M} \sigma_m u_m u_m^* \ , \qquad \textbf{6)}$$

where, **U** is a unitary matrix whose columns are the eigenvectors (u_1, u_2,…. u_M) of $\mathbf{G_{sb}}$ and **Σ** is a diagonal matrix whose diagonal elements are real valued eigenvalues (σ_1, σ_2,… σ_M) of $\mathbf{G_{sb}}$. Fig 7 shows the distribution of the eigenvalues obtained from the present test at frequencies of 510hz and 1025 Hz. Note that most eigenvalues are very small even for the distributed nature of the noise sources expected in the engine test. Because the intention was to investigate the peak noise sources within a given dB range, a threshold level can be used based on the highest eigenvalue σ_{max}. For the present application the intention was to find the sources responsible for creating at most the top 10dB range of pressure fluctuations. Therefore, all eigenvalues below the following criteria were considered due to the background noise sources and were equated to zero.

$$\sigma_m < \frac{\sigma_{max}}{40} \rightarrow 0. \qquad \textbf{(7)}$$

For the two frequencies 510Hz and 1025 Hz shown in fig 7, respectively, 6 and 12 eigenvalues were retained – rest were equated to zero. These eigenvalues, σ_s, s=1,2…S are due to the desired sound sources and were used to reconstruct the cross-spectral matrix $\mathbf{G_s}$ free of the background noise:

$$\boldsymbol{G_s = U\Sigma_S U^*}, \qquad \textbf{(8)}$$

where, $\mathbf{\Sigma_s}$ is a diagonal matrix composed of the non-zero eigenvalues, rest equated to zero. Note that this procedure of zeroing out the weaker eigenvalues were used only with the Functional beamforming. For conventional and SEM schemes the noise subtracted cross spectra of equation 5 was used.

Va. Conventional beamforming (CB):

To create maps of the noise sources at first the region where such sources are expected to be present is divided into a set of grid points. Typically, a planar phased array is insensitive in the depth direction

(i.e., along the normal to the array plane). The current hemispherical shape is expected to provide improvements, yet the large separation distance between the pad and the array location is expected to make such improvements insignificant. Therefore, a two-dimensional set of grid points (also called interrogation points) is set up. Let j =1, 2, 3…N be the interrogation points. The radial distance r_{jm}, from an interrogation point to an individual microphone, determines the phase shift and the relative amplitude measured by the microphone. The steering vector is a column matrix defined to incorporate these properties:

$$w_{j,m} = \frac{r_{jm}}{r_{jc}}\, e^{-ik\, r_{jm}} \quad \textbf{(9)}$$

Here r_{jc} is the distance of each interrogation point to the center of the array. Note that: $\boldsymbol{w}_j^{\dagger}\boldsymbol{w}_j = 1$.

The elements of the cross-spectral matrix of Equation 5 above are summed up, preceded by a phase adjustment by the steering vectors, to interrogate the individual grid points. These two steps are combined in a matrix manipulation which leads to the conventional beamform map. In the following $G_{m,m/}$ is a shorter representation of the matrix $G_{mm/,sb}$ of equation 5.

$$b_{j,cb}(f) = w_{j,m}{}^{\dagger} G_{m,m/}\, w_{j,m/} \quad \textbf{(10)}$$

Zeroing out the diagonal elements of $G_{m,m/}$ improves the beamformed map.

Vb. Modified Functional beamforming (FB):

This method proposed by Dougherty [10, 11] uses the eigenvalue and eigenvector decomposition of the cross-spectral matrix described. For the present case the electronic noise subtracted, and background noise removed cross-spectrum and its' eigenvalue decomposition of equation (8) is used. Note that the functional beamform proposed by Dougherty did not account for noise reduction via zeroing out of the smaller eigenvalues. That idea was a part of the Orthogonal beamform scheme [12modified]. Since the current method is a mix of the two so it is referred as Functional scheme. The central idea of the functional beamforming is to reduce the spot size (point-spread function) and the alias points (sidelobes – fake noise sources) by reducing the magnitude of the cross-spectral matrix via an exponent 1/v, v>1, before adjusting the phase and summing up the levels. This is followed by raising the beamformed levels back to the original. The reductions in the magnitude of the cross-spectral matrix can be accomplished by operating on the non-zero eigenvalues: $\sigma_s^{\frac{1}{v}}$. The expression for the functional beamform is the following.

$$b_{j,fb}(f) = \left[w_{j,m}{}^{\dagger} \left\{ \sum_{m=1}^{M} \sigma_s^{\frac{1}{v}} u_m u_m^{*} \right\} w_{j,m/} \right]^{v} \quad \textbf{(11)}$$

The exponent v is to be selected by the user. For a completely noise free data the dynamic range (reduction of the side lobes) and the reduction in the spot size (i.e., improvement in the resolution of the beamformed map) is directly related to v: the higher the v the smaller is the spot size, and wider is the

dynamic range. In practice the residual noise level, and the lack of convergence due to the limited time extent of the microphone data, plateau the spot size to a fixed level. Typically, v in the range of 10 to 100 is used in the literature. Marino-Martinez et. al. [10] found an improvement of the array resolution by a factor of 6 compared to the conventional beamformed value by applying v=100 to clean data from an airframe noise test. It was observed that the absolute beamform levels were much lower than that found from the conventional beamform. As v is increased and more of the lower eigenvalues neglected the discrepancies grew larger. Therefore, the peak beamform levels from the FB scheme were adjusted to that calculated from the CB scheme. In other words, calculations for the functional beamform needed to be preceded by the conventional one.

Vc. Direct Spectral Estimate – Spectral Element Method (SEM):

The resolving capability and the dynamic range available by a phased array of a given size and given number of microphones are limited by the 3dB width of the psf. As discussed earlier the point-spread function and the sidelobe makes a point source of sound to appear over a wide spatial extent and at pseudo locations. The functional beamform do makes significant improvements of the resolvability, but the best results can be obtained if the point-spread function can be deconvolved out of the beamform maps. There are a host of different schemes available [13] towards that end. An important limitation of many such schemes is that they break down a distributed source into small points which makes them to appear unphysical. The spectral element method also suffers from this limitation but to a lesser extent [13]. Like others SEM also assumes that the sound sources are made of uncorrelated monopoles. However, instead of making phase adjustment via the steering vectors the method attempts to find the strength of the monopoles directly from the measured cross-spectral matrix $\mathbf{G_{sb}}$. Like before the source region is divided into N_s interrogation points (also called grid points) and the steering vectors are used to calculate a model of cross-spectrum between two microphones m and m/. The unknown in the model is the strength of the monopole sources α_j^2 at each of the interrogation point j = 1, 2 … N_s. The model cross-spectrum between microphones m and m/ is the following.

$$G_{mm/}^{mod} = \sum_{j=1}^{N} w_{j,m}\alpha_j^2 w_{j,m/}^{*} = \sum_{j=1}^{N} \left(\frac{r_{jm}}{r_{jc}}\, e^{-ik\, r_{jm}}\right) \alpha_j^2 \left(\frac{r_{jm/}}{r_{jc}}\, e^{-ik\, r_{jm/}}\right)^{*} \quad \textbf{(12)}$$

The positive values of α_j^2 assure elimination of the unphysical negative source strength. In the method proposed by Blacondon & Élias [14] the source distribution is determined via minimization of the error between the measured and the modeled cross-spectra using an iterative least-square minimization scheme.

$$E(\alpha_j, f) = \sum_{m,m/=1}^{J} \left| G_{mm/} - \sum_{j=1}^{N} w_{j,m}\alpha_j^2 w_{j,m/}^{*} \right|^2 \quad \textbf{(13)}$$

An advantage of the SEM is that the diagonal terms of the measured cross-spectrum can be avoided in the minimization scheme. Without the diagonal terms the measured cross-spectral matrix $\mathbf{G_{sb}}$ contains

(M^2-M)/2 number of independent, complex values. Counting the imaginary and the real numbers separately, the total number of independent variables to be minimized becomes *J*.

$$J = M^2\text{-}M \quad \textbf{(14)}$$

Similar to a procedure followed by Casalino et al [15], the calculations were carried out in Matlab® using routine *lsqnonneg* that uses a non-negative least square process.

Vd. Matlab® implementation:

The above beamforming schemes were implemented in the commercially available Matlab® platform. Once the cross-spectral matrix (Eq 8) was calculated the rest of the beamforming operation for conventional, functional and SEM methods happened quickly. To facilitate direct identification of the noise sources, the interrogation grid was created over a photograph of the region of interest captured via either the visible band or the infra-red band video camera. The photographed region was divided into a uniformly spaced grid. To select the number of grid points, Rayleigh criterion was applied to the highest frequency of interest. Typically, the grid spacing obtained by Rayleigh criterion was refined by a factor of 10. The beamformed colored maps were superimposed on a video frame from either the visible band or the IR-band camera. Implementation of SEM typically required fewer grid points.To limit the computing time to a reasonable duration, the maximum number of iterations in *lsqnonneg* routine was limited to 500.

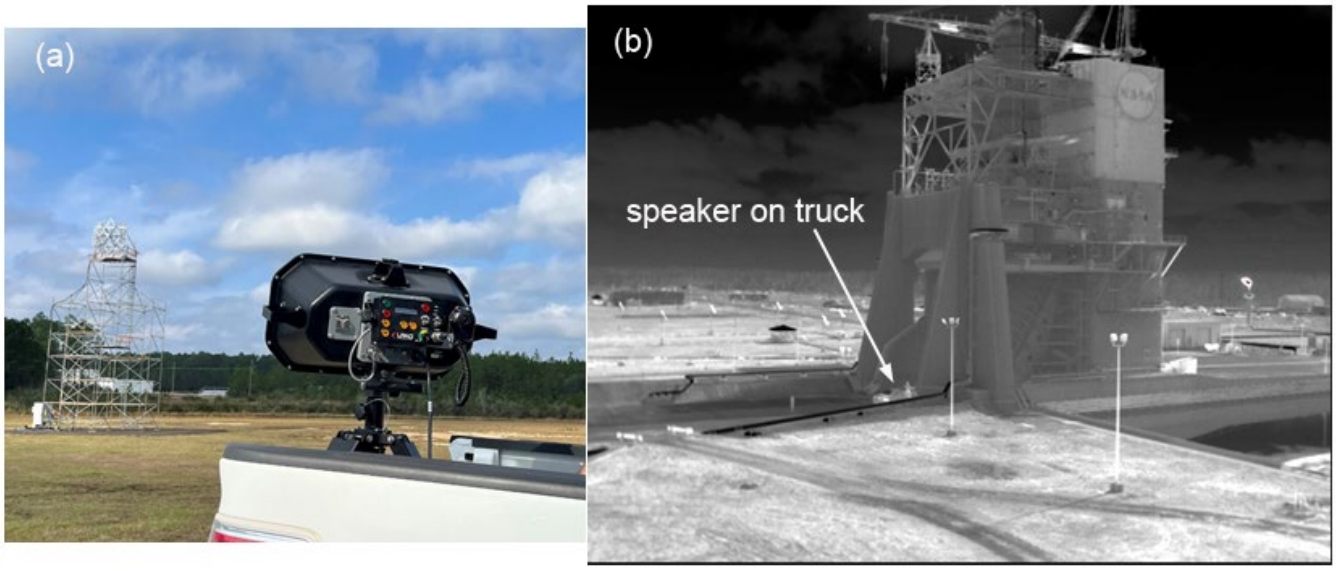

Fig 8. (a) Photograph of the speaker pointing towards the array; (b) photo from the IR camera locating the speaker.

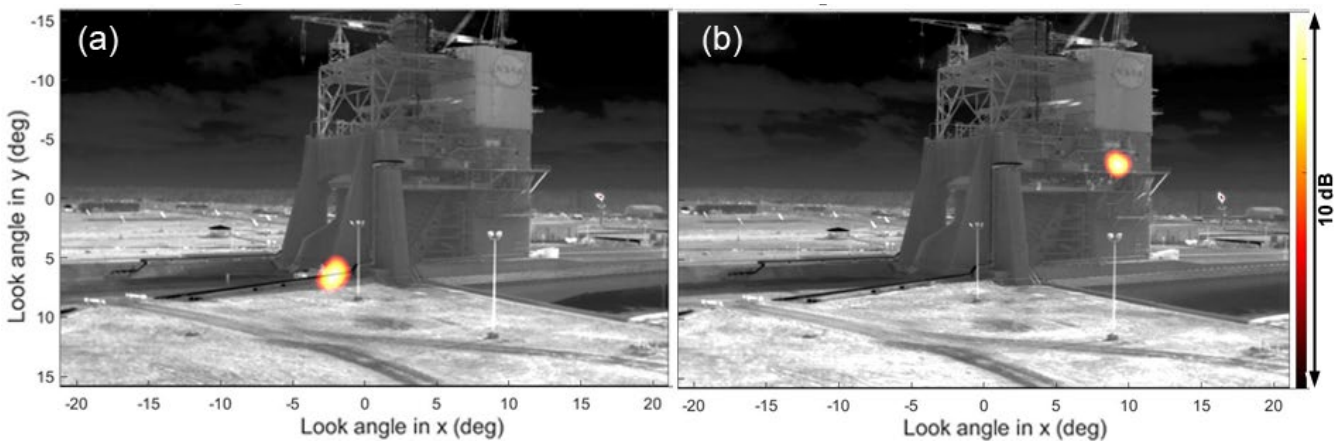

Fig 9. Identification of the speaker locations via beamform maps. Speaker located at (a) the base of the deflector (same as fig 8b above); (b) on deck 4.

VI. RESULTS

VIa. Validation of the phased array operation via identification of a single speaker source

Correct registration of the beamformed map and the video frames required a calibration process. The look-angle of the video camera changed slightly every time the array was rebuilt. To correct for such a small but important change, a speaker was placed at various locations in the camera field of view, and the video image was rotated in pitch, yaw and/or roll directions for correct superposition of the beamformed maps. These are the first series of test conducted days before the engine burn – just after lifting and securing the array on the scaffold structure. A high intensity speaker (Long Range Acoustic Device, LRAD) was mounted on the bed of a truck and was placed at multiple locations around the test site (fig 8a), and on the test stand. The cameras inside the array canister were used to photograph the speaker location (fig 8b) and the acoustic data recorded. The beamformed map superimposed on the camera images were used to determine the slight tilt angles of the camera with respect to the array axis and to verify the camera calibration. The speaker produced sharp tones mostly >1 kHz frequencies. Fig 9 shows sample beamformed maps at 3 kHz superimposed on a frame of the IR camera for two different speaker positions. Similar maps were created for all other speaker locations. All maps were created using the Functional-Orthogonal scheme using v = 20.The look angles were calculated from the center of the image and adjusts for the camera tilt angles. The color scale on the right shows the top 10dB range of the beamformed map used for plotting. Correct juxtaposition of the beamformed map on the speaker verified the calibration and brought confidence on the accuracy of noise maps created by the array.

VIb. RS-25 static burn

The phased array was used during the hot-fire test of a redesigned Rs-25 engine on Dec 14, 2022. The engine would be used in the future Artemis missions. Microphone data and camera images were

collected for the entire test duration of 209s. The array hardware were setup five days prior to the actual burn and was exposed to high wind, multiple thunderstorms, and wind driven rain for four consecutive days. The exposure to the weather element was also a part of the validation test. Two of the 70 microphones showed unstable signal due to exposure to moistures, and were unusable. The rest of the instruments worked without any issue for the entire duration.

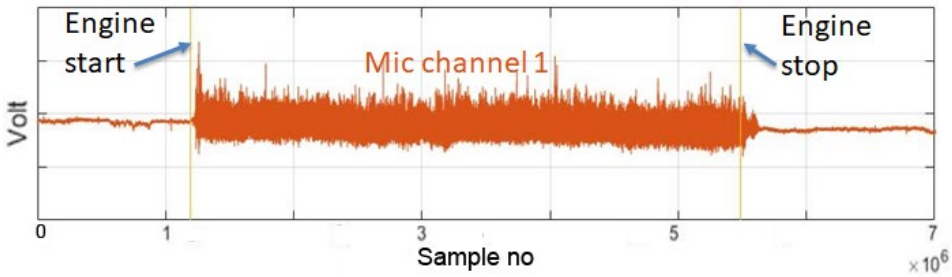

Fig 10. Time trace of a microphone signal.

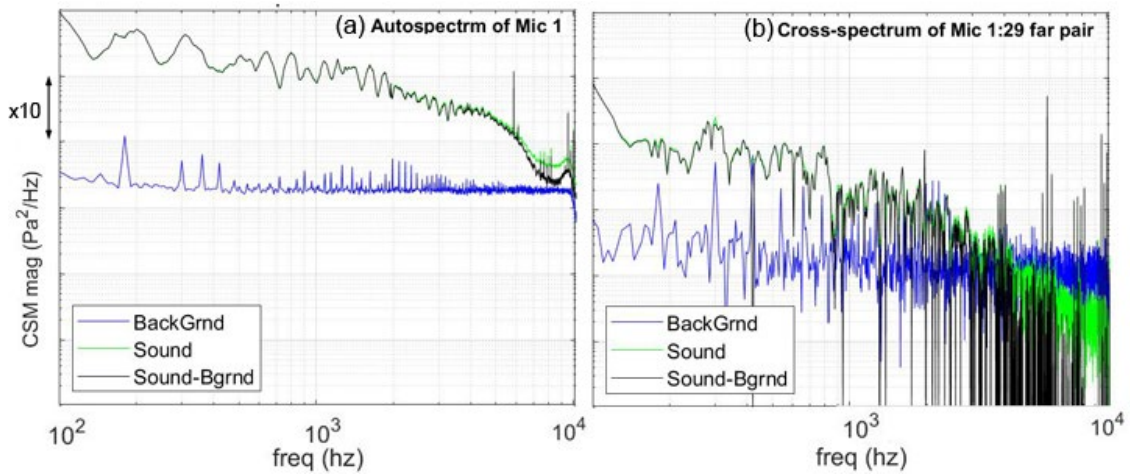

Fig 11. (a) Auto and (b) cross-spectra from the indicated microphone and microphone pairs.

Figure 10 shows a sample time series from the microphone no 1 along with the engine start and stop signal. The microphone data was collected at a rate of 20480 sample/s. An examination of fig 10 shows signal level higher than the background noise floor but significantly weaker than the expected level from a Artemis launch. The lower level is expected since only one engine - out of 4 liquid engines and two solid boosters – were used in this test. Nonetheless, the longer duration signal provided good data for beamforming. The time series was truncated and data from the duration of the test was used to calculate auto and cross-spectra. Fig 11 shows an auto and a cross-spectra and the impact of background subtraction (eq. 5). The background subtraction was found to affect mostly the high frequency (>2.5 kHz) part of the cross-spectrum. Another interesting observation is that the energy in

the cross-spectra were mostly confined to the lower frequency end <3 kHz. It is suspected that the high amount of water injection attenuated the high frequency part of the acoustic spectrum.

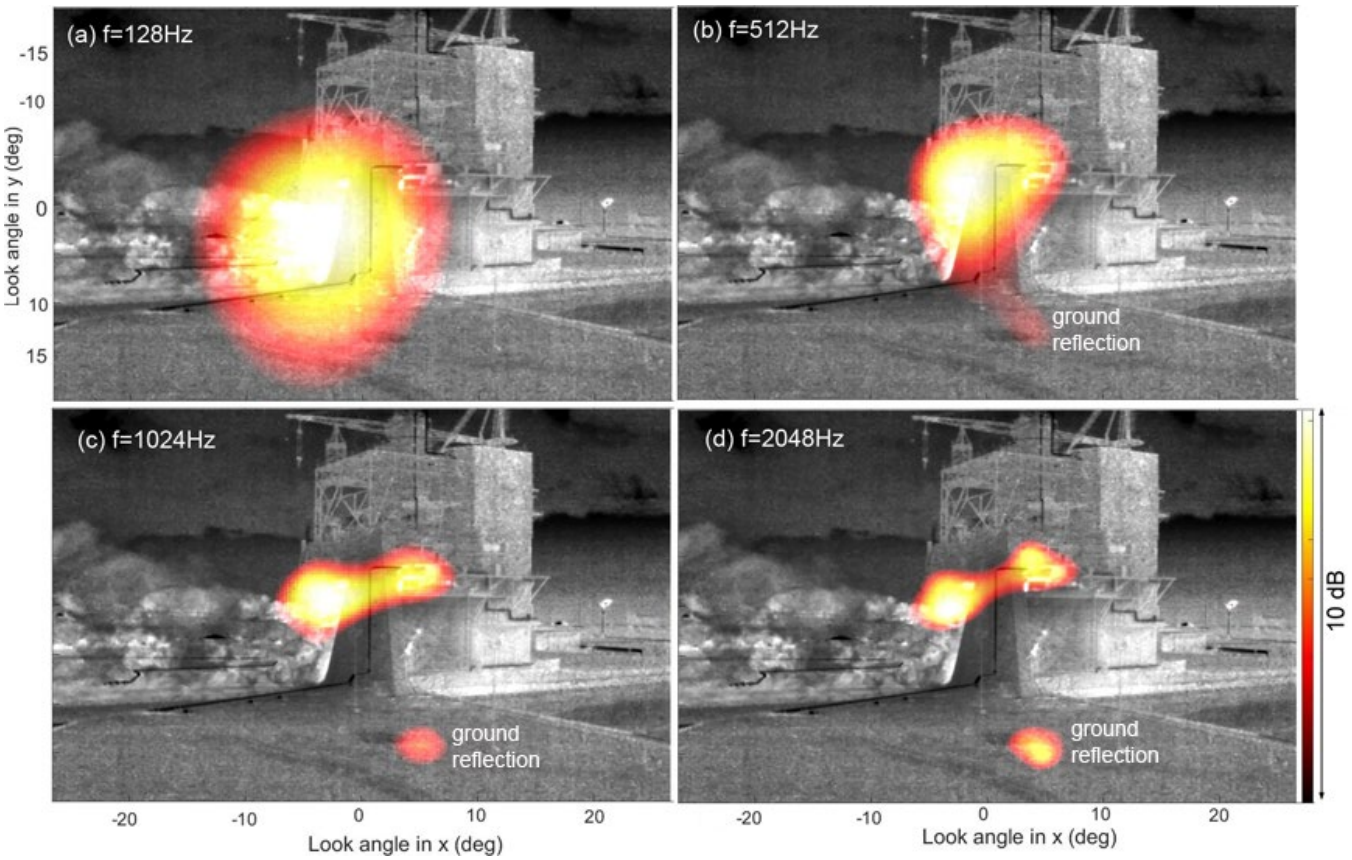

Fig 12. Noise sources identified at the indicated third-octave center frequencies, functional-orthogonal beamform, nu=20.

VIc. Noise sources identified through third octave beamform maps:

Figure 12 shows the beamformed source maps at four different frequencies obtained using Functional-Orthogonal method with v = 20. The frequencies are the third-octave center frequencies. Similar maps at two other frequencies are shown below in fig 13. Once again only the top 10dB range of the beamformed levels are plotted on one of the IR camera images collected during the RS-25 burn. An examination of figure 12 shows that fundamentally there are two noise sources: the flame deflector and the gap in decks 4 and 5 of the test stand. A compact region on the ground in front of the test stand also shows up in the noise maps, but this is interpreted as a reflection of the actual source on the test stand. The sound waves generated from the test stand have two different paths to reach the array: via direct propagation and via reflection on the ground. The solid ground acts as an acoustic mirror with varying reflectivity. The location of the sound reflection – marked as the ground reflection - rightfully shows up in the noise maps and ought to be ignored for source interpretation.

The plume out of the aspirator deck plunges on the deflector making the deflector as the primary source at all frequencies. At the lower frequency where the acoustic sources are expected to be wider the entire deflector brightens up as the source. As noted earlier the large amount of water injection significantly attenuates the high frequency sound. Sound maps at 1 kHz and above shows the top part of the deflector to be primary source. Noise form the plume shear layer, yet to be quenched by the water flow, is believed to be the source that radiates out from the top of the deflector. The same is believed to be cause for openings of the 4th and the 5th deck to appear as the high frequency noise source. The shear layer from the nozzle exit and various vibration induced noise from the engine emanates out of these openings making them as the noise sources.

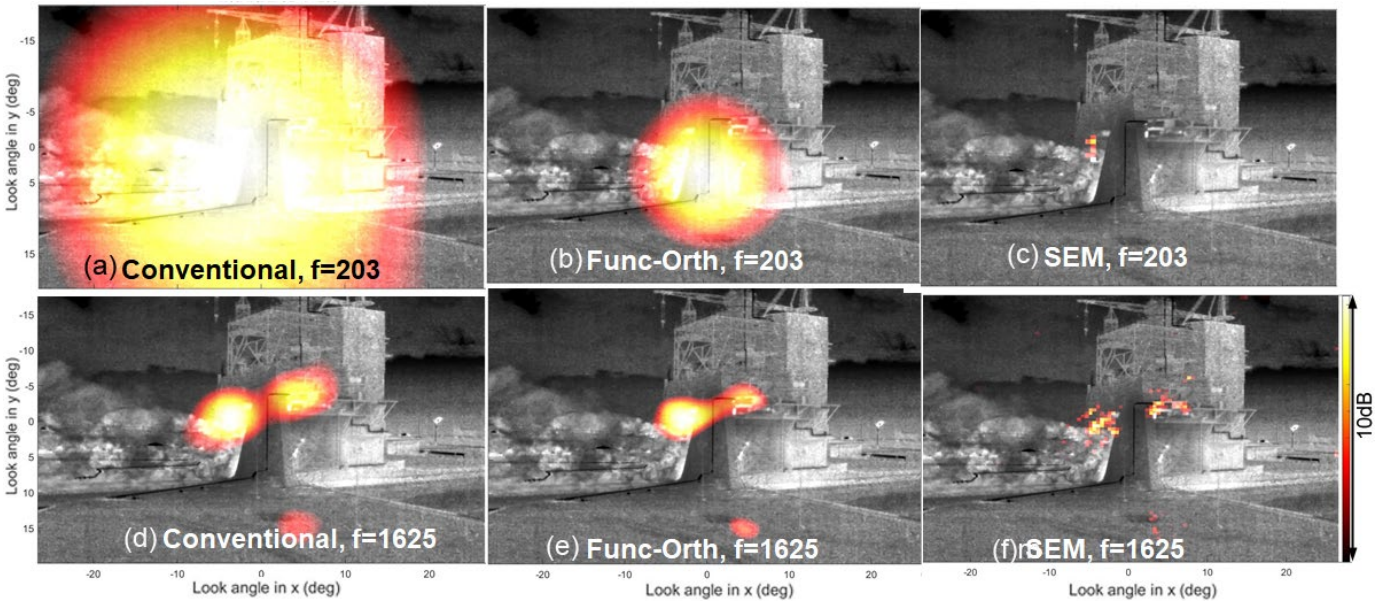

Fig 13. Comparison of 10dB spot size using the indicated scheme and at the indicated frequencies.

VId. Comparison between beamform schemes:

Fig 13 shows a comparative study of the spot sizes for two different third-octave center frequencies using the three different beamforming schemes. The large spot size of the CB map of fig 13(a) and 13(d) followed the expected Rayleigh criteria. The FOB map of fig 13(b), and 13(e) used v = 20 and is found to reduce the spot size. However, the reduction was found to be frequency dependent. For the lower 203Hz the reduction was by a factor of 3. That for the higher 1625 Hz is perhaps by a factor of 1.5. The CB has lower resolution (larger spot size) for the lower frequencies and the improvement of resolution via the FOB scheme is particularly encouraging. The SEM maps of fig 13(c) and 13(f) farther reduced the beamformed maps to a distribution of very small spots. Such a breaking down of the noise maps into small spots were also observed in the past for other deconvolution schemes.

VII. SUMMARY AND CONCLUSION

A new, portable, phased array of microphones is built at NASA Ames Research Center specifically for the harsh environment encountered in launch pads of rocket vehicles. The 70-microphone array was built on a 10.5ft diameter open frame dome structure, which was light yet robust to sustain the high wind load of typical seaside launch pads, and the blast and acoustic loads from the launch. A 200-ft long cable bundle carries the microphone signals to a weather-protected cabinet containing the data systems and allows for the placement of the array on tall structures. The array was tested during an RS-25 Engine test at the Fred Haise A-1 test stand of NASA Stennis Space Center. The engine was held vertically, and the hot plume came down on a deflector which was supplied with heavy water flow for thermal protection. Subsequently the plume and steam flowed horizontally on an open trench. The array was elevated 50ft above ground on scaffold structure, which was erected 460ft away from the test stand.

At first a set of validation tests was conducted using a high intensity single speaker positioned at many locations on and around the test stand. Correct superimposition of the beamform maps on the speaker location brought confidence on the accuracy of the noise maps. Before the actual engine test all the array hardware, except for two of the microphones, survived through four days of rain, thunderstorm and high wind. This proved the feasibility of using the array with rocket launches where prolonged exposure to the outdoor elements are expected. Good quality microphone data was collected from the test.

The data processing was conducted using three different beamforming schemes: conventional, functional-orthogonal and SEM with a goal of improving the resolution of the beamformed map. To reduce the impact of the electronic noise at first a background subtraction process was employed on the calculated cross-spectrum. Additionally, the weaker eigenvalues of the cross-spectrum were zeroed out to farther reduce the impact of noise. The functional-Orthogonal beamform was found to reduce the spot size by a factor of three, at the desirable low frequency end of spectrum.

The beamformed noise maps provided interesting insights into the sound sources on the test stand. It was found that the deflector at the bottom of the test stand was the primary noise source. For the low frequencies the entire deflector is the noise source. Impingement of the engine plume on the deflector is the cause of noise generation. Huge amount of water injection particularly attenuated the high frequency part of the spectra. The openings in the nozzle and aspirator decks were found to be the other noise sources. The noise generated from the plume shear layer and engine vibrations were radiated out of these openings. Interestingly, unlike the expectations from standard models [1] the flume through which the plume and the steam mixture flowed downstream was not found to contribute

towards the top 10dB of noise sources. We believe that the noise maps presented in this report are first such measurements from a full-scale rocket engine test stand.

Acknowledgements:

The authors are thankful to NASA Engineering and Safety Center (NESC) for supporting the building of the hardware and performing the verification and validation tests. Help from many technicians and support staff of NASA SSC for lifting and mounting of the array played a vital role. We also acknowledge help from Mr. Mike Smiles, NESC chief engineer at SSC in coordinating the Stennis activities. Mr. David Keil of Jacobs, Mr. Matt McKay of NASA Ames, and Mr. Rene Formoso and Mr. Malay Shah of NASA Kennedy Space Center participated in various preparatory and data collection stages of the operation.

References:

[1] Eldred, K. M. & Jones, G. W., Jr., “Acoustic load generated by the propulsion system,” NASA SP-8072, 1971.

[2] Panda, J. & Mosher, R., “Microphone Phased Array to Identify Liftoff Noise Sources in Model-Scale Tests,” Journal of Spacecraft and Rockets, Vol. 50, No. 5, Sept-Oct 2013. DOI: 10.2514/1.A32433

[3] Panda, J., Mosher, R. N. & Porter, B. J., “Noise Source Identification during Rocket Engine Test Firings and a Rocket Launch,” Journal of Spacecraft and Rockets, Vol. 51, No. 4, July-Aug 2014. DOI: 10.2514/1.A32863.

[4] Gély, D., Elias, G., Bresson, C., Foulon, H., Radulovic, S, 2000 “Reduction of supersonic jet noise. Application to the Ariane 5 launch vehicle,” 6th AIAA/CEAS Aeracoustics Conference, AIAA paper 2000-2026, 2000.

[5] Mortain, F. & Clero, F., “Full-scale acoustic source identification on Vega Launch pad at lift-off”, 26th Intl. Congress on Sound & Vib., July 2019.

[6] 88. Panda, J., Nguyen, M. P., Keil, D. R., Hamm, K. R. Jr., “A Microphone Phased Array for Launch Acoustics Application,” presented at AIAA SciTech Forum, 23-27 Jan. 2023, National Harbor, MD; AIAA paper 2023-0790.

[7] Burnside, N. J. & Horne, W. C., “Development of Instrumentation and Methods for Time-Domain Measurement of Rotor-Type noise Sources in a Hard Wall Wind Tunnel,” presented at the VFS Aeromechanics for Advanced Vertical Flight Testing Meeting, San Jose, CA, Jan. 21-23, 2020.

[8] https://www.nasa.gov/sites/default/files/atoms/files/fred_haise_test_stand_v1.pdf

[9] Bahr, C.J., Horne, W. C.: Subspace-based background noise subtraction applied to aeroacoustic wind tunnel testing. Int. J. Aeroacoust. 16(4–5), 299–325, 2017.

[10] Dougherty, R.P., “Functional Beamforming”, Berlin Beamforming Conference, BeBeC 2014-1, 2014.
[11] Dougherty, R.P., "Functional Beamforming for aeroacoustic source distributions", AIAA Paper 2014-3066, 2014.
[12] Sarradj, E. “A fast signal subspace approach for the determination of absolute levels from phased microphone array measurements,” *J. Sound & Vib.,* vol. 329, pp. 1553-1569, 2010.
[13] R. Merino-Martinez, P. Sijtsma, M. Snellen, T. Ahlefeldt, J. Antoni, C.J. Bahr, D. Blacondon, D. Ernst, A. Finez, S. Funke, T.F. Geyer, S. Haxter, G. Herold, X. Huang, W. M. Humphreys, Q. Leclere, A. Malgoezar, U. Michel, T. Padois, A. Pereia, C. Picard, e. Sarradj, H. Siller, D.G. Simons, C. Spehr, “A review of acoustic imaging methods using phased microphone arrays,” CEAS Aeronautical Journal, 10:197-230, 16 March 2019.
[14] Blacondon, D., & Élias, G., “Level Estimation of Extended Acoustic Sources Using a Parametric Method,” J. Aircraft, vol. 41, no. 6, pp. 1360-136, Nov.-Dec. 2004.
[15] Casalino, D., Santini, S., Genito, M., and Ferrara, V., “Rocket Noise Sources Localization through a Tailored Beam-Forming Technique,” *AIAA J.*, Vol. 50, No. 10, Oct. 2012, pp. 2146–2158. doi:10.2514/1.J051479